https://doi.org/10.1016/j.ensm.2021.07.009

Multi-Scale Uniform Li Regulation Triggered by Tunable Electric Field Distribution on Oxygen-Functionalized Porous Framework for Flexible Li-S Full Batteries

Yue Ouyang[a,†], Wei Zong[a,†], Jing Wang[c], Zhen Xu[d], LuLu Mo[a], Feili Lai[e], Zheng-Long Xu[b], Yue-E Miao[a,*], and Tianxi Liu[a,*]

[a] State Key Laboratory for Modification of Chemical Fibers and Polymer Materials, College of Materials Science and Engineering, Innovation Center for Textile Science and Technology, Donghua University, Shanghai 201620, People's Republic of China

[b] Department of Industrial and Systems Engineering, The Hong Kong Polytechnic University, Hong Hum, Kowloon, Hong Kong

[c] Bristol Composites Institute (ACCIS), Department of Aerospace Engineering, Queen's Building, University of Bristol, University Walk, Bristol, BS8 1TR, United Kingdom

[d] Department of Chemical Engineering, Imperial College London, London, SW7 2AZ, United Kingdom

[e] Department of Chemistry, KU Leuven, Celestijnenlaan 200F, Leuven 3001, Belgium

* Corresponding authors.

E-mail address: yuee_miao@dhu.edu.cn (Yue-E Miao) or txliu@dhu.edu.cn (Tianxi Liu)

† These authors contributed equally.

Abstract: Lithium-sulfur (Li-S) batteries with high theoretical energy densities have long been identified a promising energy storage system. Nonetheless, it is not trivial to simultaneously achieve dendrite-free lithium metal anode and stable sulfur cathode for practical applications. To tackle this issue, we herein design an oxygen-functionalized mesoporous carbon nanofiber framework decorated with well-distributed nickel nanoparticles as bifunctional hosts for both electrodes. The combined theoretical and experimental results reveal that the regulated electric field stemming from the oxygenated and mesoporous structure can effectively facilitate the uniform nucleation and growth of dendrite-free Li metal in local nanofiber and whole electrode levels. Meanwhile, the strong affiliation of oxygenated groups to lithium polysulfides greatly alleviate the shuttle effect, leading to impressive cyclic stability. When coupling above optimal electrodes into a flexible Li-S full battery with an ultralow negative to positive capacity ratio of 2.0, the new battery presents remarkable electrochemical performance with a high rate capability of 882 mAh g^{-1} at 2.0 C and an extremely low capacity decay rate of 0.005% per cycle over 300 cycles. The stable electrochemical performance exhibited by a flexible Li-S battery under different mechanical deformations paves the way for future practical applications in flexible energy storage devices based on the bifunctional hosts.

Keywords: Carbon nanofibers; Bifunctional hosts; Dendrite-free; Tunable E-field distribution; Flexible Li-S full batteries

1. Introduction

Over the past years, the rising of novel intelligent electronics like roll-up displays and smart textiles have created increasing demands for lightweight and flexible rechargeable batteries which are expected to possess superior energy density to the conventional lithium-ion batteries [1-4]. Lithium-sulfur (Li-S) batteries, based on the redox reactions of lithium metal anode and sulfur cathode, have been regarded as one of the most promising candidates with an ultrahigh theoretical energy density of 2600 Wh kg^{-1} [5-7]. Noteworthy is that the lithium metal is an ideal anode to Li-S batteries, due to its remarkably high theoretical specific capacity of 3860 mAh g^{-1}, a low gravimetric density of 0.534 g cm^{-3} and a low electrochemical potential of -3.04 V *versus* standard hydrogen electrode [8-10]. Furthermore, the eco-friendly elemental sulfur shows great market potentials with multi-advantages of ultrahigh theoretical specific capacity (1675 mAh g^{-1}), natural abundance and low cost [11-13].

However, practical implementation of Li-S batteries has been hindered by a multitude of fundamental challenges. On one hand, the lithium metal anode has been troubled with lithium dendrite growth, unstable solid electrolyte interphase (SEI) and poor cyclic stability, arising from its high chemical reactivity and host-less essence [14-16]. Li dendrite growth is ready to induce internal short circuit and devastate safety concerns during repeated Li plating/stripping processes, especially at high working rates [17,18]. On the other hand, the sulfur cathodes present unsatisfactory electrochemical capability because of the insulating nature of sulfur and lithium sulfides, the large volumetric change of sulfur (≈ 80%) during discharge/charge, and shuttling

effect of the reaction intermediates, lithium polysulfides (LiPSs). Consequently, the electrochemical performance of sluggish redox kinetics, low active material utilization, fast capacity attenuation and poor cycling life are observed for Li-S batteries [19-22]. As the heavy demands for flexible energy storage systems [23-26], it is highly necessary to design the bifunctional flexible host with simultaneously improved electrochemical performances for both dendrite-free anode and LiPSs-anchored cathode.

Self-standing carbon-based materials like carbon nanofiber membranes have been regarded as one of the most promising carriers, on account of their excellent mechanical integrity, superior electron conductivity and reproductive preparation processes [17,27-30]. Besides, its three-dimensional (3D) open framework with high porosity can also benefit ion transport and minimize the volume change from active materials upon long-term cycling [31-33]. However, the severe LiPSs shuttle cannot be totally suppressed by the physical confinement of porous structure. On Li anode side, the aggregated electric field (E-field) and shorten Li^+ diffusion pathway offered by the 3D conductive framework will drive the preferential initiation/growth of Li metal on the upper region which is called “top-growth” mode. The surface accumulation of Li metal/dendrites close to the anode/separator interface will cause early cell failure [34-37]. In terms of the interconnected nanofibers within the framework, lithium tends to deposit on the junctions of fibers with significantly higher E-field instead uniformly on the fiber surface, which results in abundant dead Li with a reduced Coulombic efficiency [33,38]. Apparently, the E-field distribution for the 3D conductive framework is of essentially importance in guiding the electrochemical deposition of Li metal, which is far from

satisfactory at current stage to ensure stable Li anodes.

Herein, we report an oxygen-functionalized 3D mesoporous carbon nanofiber framework with well-distributed nickel nanoparticles (Ni@PCNF-O) as bifunctional hosts for both lithium metal anode and sulfur cathode. Apart from the large volume changes of Li and S can be alleviated by the flexible 3D porous structure during cycling, the oxygen groups and rich mesopores are able to tune the electric field distribution via simultaneously reducing the whole electrode conductivity and optimizing nanofiber surface structure, thus regulating Li metal deposition in a smooth and dendrite-free manner. Meanwhile, the Ni@PCNF-O composite can serve as the strong adsorbent to inhibit LiPSs diffusion in the sulfur cathode. Benefitting from both the dendrite-free Li deposition and enhanced sulfur utilization, the coupled Li-S full batteries deliver excellent rate performance of 882 mAh g^{-1} at 2.0 C and long cycling stability of only 0.005% decay per cycle over 300 cycles at 1.0 C. The stable electrochemical performance exhibited by a flexible Li-S battery under different mechanical deformations paves the way for future practical applications in flexible energy storage devices based on the bifunctional hosts.

2. Results and Discussion

2.1 Multi-Scale Uniform Li Regulation by the Oxygen-Functionalized Porous Framework

Due to its infinite volume change and high chemical/electrochemical reactivity, the hostless metallic Li prefers uneven deposition and then forms dendrites during

plating/stripping processes, eventually leading to fast capacity fading and safety hazards. Considering the highly interconnected conductive network which can facilitate rapid electron transport and alleviate large volume expansion of Li metal upon cycling, a 3D carbon nanofiber framework with well-distributed nickel nanoparticles (Ni@CNF, Fig. S1) was initially proposed to host Li metal anode as illustrated in Fig. 1a. Nonetheless, the *COMSOL* Multiphysics simulation reveals that the E-field is concentrated on the upper area of Ni@CNF composite (Fig. 1c), which will lead to the asymmetric deposition of Li on the top section of the Ni@CNF electrode, and finally results in uncontrollable Li dendrites shown in Fig. 1a.

In order to inhibit the top-growth of Li metal, the Ni@CNF composite is further treated under O_2 microwave plasma to obtain the oxygen functionalized carbon nanofiber framework with Ni nanoparticles (Ni@CNF-O). According to the simulation of the electric field in Ni@CNF-O electrode (Fig. 1d), the polarization of E-field reduces after the introduction of oxygenated groups. This can be attributed to the decreased conductivity and increased electron transport barrier in the whole electrode region. Furthermore, the cross-sectional E-field profiles along the normal Z direction of the electrode similarly imply a smaller electric field intensity differential within the 3D Ni@CNF-O electrode (Fig. 1e), which is beneficial to homogenous lithium deposition. In the mid to late Li deposition period, the Li^+ concentration plays a more dominant role than the electric field. Compared to the typical concentration polarization of the Ni@CNF electrode, the Ni@CNF-O electrode displays a smaller Li^+ concentration gradient in the simulation diagram of Li^+ flux distribution (Fig. S2).

Additionally, the oxygen groups can effectively improve the lithiophilicity of the carbon framework (Fig. S3), further contributing to the uniform and dendrite-free Li deposition.

As aforementioned, another challenge to realize uniform Li deposition lies in the interconnected nanofibers within 3D conductive frameworks. To prevent the preferential plating of Li at the junctions of Ni@CNF nanofibers, mesoporous structure has been introduced to Ni@CNF nanofiber surface by adding pore-forming agent to form mesoporous Ni@CNF, which is designated as Ni@PCNF. As simulated in one simplified porous nanofiber during Li deposition (Fig. 1f), the pore edges present the higher current density because of the larger curvature based on the classical "lightning rod theory", which also correspond to the favorable electrochemical reactivity for Li deposition [39, 40]. As the further plating continues, Li distribution spreads from the outermost circle, following the flow lines of Li ion flux movement (Fig. 1g), into the pores with denser lines until all the pores are filled, as illustrated in Fig. 1h. Abundant mesopores on the Ni@PCNF nanofiber surface are beneficial to act as the active sites for Li nucleation/growth, thus gradually forming a dense lithium layer around the interconnected nanofibers. Hence, an oxygen-functionalized 3D mesoporous carbon nanofiber framework with well-distributed nickel nanoparticles (Ni@PCNF-O) is rationally designed with oxygen groups as well as mesoporous structure, which are expected to achieve the tunable E-field and Li-ion flux distribution to regulate the uniform Li deposition at whole electrode and local nanofiber scales (Fig. 1a).

2.2 Preparation and Characterization of Ni@PCNF-O Composite

To fabricate the Ni@PCNF-O composite, a simple but rationally designed route including electrospinning, carbonization and O_2 plasma processes is conducted (Fig. 2a), to achieve the dual-functional flexible nanofibrous membrane host (Fig. S4) for multi-scale uniform deposition of lithium and efficient immobilization of LiPSs. As shown in the scanning electron microscopy (SEM) image of Fig. 2b, the Ni@PCNF-O composite exhibits fibrous morphology with uniform size. The Ni nanoparticles embedded carbon nanofiber membrane also displays high flexibility (inset in Fig. 2b). The transmission electron microscopy (TEM) image and corresponding energy-dispersive X-ray spectroscopy (EDX) clearly show that Ni nanoparticles with an average diameter of about 10 nm are evenly distributed within the carbon nanofiber matrix (Fig. 2c, 2d). X-ray diffraction (XRD) (Fig. S5) and X-ray photoelectron spectroscopy (XPS) characterizations (Fig. S6a) further validate the incorporation of Ni nanoparticles. The Ni content is determined to be 19.4 wt% from the thermogravimetric analysis (TGA) in Fig. S7. Under TEM observation, abundant mesopores can be clearly observed in Ni@PCNF-O nanofibers (Fig. 2e). The porosity is further quantitatively characterized by Brunauer-Emmett-Teller (BET) with a notably high surface area of 153.3 $m^2 g^{-1}$ (Fig. 2f), and the pore size is mainly located from 4 to 10 nm, consistent with the TEM image. The exceptionally high surface area and large pore volume (0.288 $cm^3 g^{-1}$) of Ni@PCNF-O composite are expected to lower the local current density for steady lithium deposition and physically confine LiPSs within each nanofiber. Furthermore, O_2 plasma treatment is carried out to decrease the conductivity of Ni@PCNF matrix and achieve the uniform Li deposition in the whole electrode scale.

Compared with Ni@PCNF without O_2 plasma, the oxygen content sharply rises from 4.1% to 12.7% as indicated by XPS (Fig. 2g), together with the peaks of carbonyl oxygen (533.2 eV) and hydroxyl oxygen (531.2 eV) appear in the high-resolution O 1s spectra (Fig. S6b), which verifies the introduction of functional oxygen groups in Ni@PCNF-O composite [41]. Furthermore, the in-plane conductivity decreases from 10.5 S cm^{-1} of Ni@PCNF to 2.6 S cm^{-1} of Ni@PCNF-O under a four-probe tester (Fig. S8).

2.3 Li Metal Plating/Stripping Behaviors in Ni@PCNF-O Composite Host

The optimized Ni@PCNF-O composite membrane is directly applied as a 3D scaffold to accommodate Li metal without additional current collectors. The Li plating/stripping on Ni@CNF and conventional copper (Cu) foil current collectors are also investigated as comparisons. As observed by the in-situ optical microscopy (Fig. 3a, 3b and S9), the operando cells without conventional polymer separators are assembled using different substrates and bare Li which act as the working and counter electrodes, respectively. Under a plating current density of 4 mA cm^{-2}, the visible formation of Li dendrites on Cu foil appears only after 7 min, and Li dendrites continue to grow close to the anode in 10 min (Fig. S9). When lithium is deposited on Ni@CNF electrode (Fig. 3a), the Li layer gradually loosens after 10 min and obvious dendrites appear in 15 min. On the contrary, the deposited Li uniformly emerges on the pristine Ni@PCNF-O electrode with a thickness of ~80 μm during the first five minutes of deposition (Fig. 3b), suggesting a successful regulation of Li metal plating. The following deposited Li gradually extends from vast existing sites (7 min), and then

homogeneously wraps on the Ni@PCNF-O electrode upon further plating (10 min). After 30 min of Li loading, the Ni@PCNF-O composite with deposited Li (Ni@PCNF-O@Li) expands to ~100 μm, but still remains compact and dendrite-free. Fig. 3c and 3d show the optical images of the Li-deposited Ni@CNF (Ni@CNF@Li) and Ni@PCNF-O@Li electrodes with 3 mAh cm^{-2}. The distinct color change from Ni@CNF to Ni@CNF@Li indicates that Li is plated in the top region of Ni@CNF composite which is close to the separator due to the severe E-field polarization. By contrast, Li is deposited uniformly within the whole Ni@PCNF-O composite without any color change, implying the "top-growth" mode is effectively relieved.

Meanwhile, the nanoscale morphology evolution with various areal capacities of deposited Li on different substrates is explored by SEM. As shown in Fig. S10, with the plating current density of 1 mA cm^{-2}, the surface of Cu substrate is covered with massive uneven dendritic Li with the length of over tens of micrometers even after the first plating. In the case of neat Ni@CNF substrate (Fig. 3e, S11a and S12a), Li tends to nucleate and grow on the junctions of the interconnected Ni@CNF nanofibers due to its uneven E-field distribution (Fig. $3e_1$). After plating with 8 mAh cm^{-2} of Li, it can be observed that mossy Li aggregates heavily on the top surface of the Ni@CNF composite membrane instead of filling inside the whole carbon nanofiber matrix (Fig. $3e_2$ and S12a). In sharp contrast, the surface of Ni@PCNF-O@Li composite membrane obviously demonstrates much smoother morphology without Li dendritic formation (Fig. 3f, S11b and S12b), which demonstrates the well-guided Li deposition contributed by the rich mesopores on the nanofiber surface and improved lithiophilicity as well.

With the increasing Li plating capacities to 2 mAh cm^{-2} and 8 mAh cm^{-2}, the diameter of Ni@PCNF-O@Li nanofibers increases to 240 nm (inset of Fig. $3f_1$) and 530 nm (inset of Fig. $3f_2$) respectively compared to that (200 nm) of the original nanofibers, illustrating a flat lithium coating layer formed on the surface of Ni@PCNF-O nanofibers. Therefore, the Ni@PCNF-O composite deposited with 8 mAh cm^{-2} of Li still shows denser morphology without any apparent mossy or dendritic Li in the cross-sectional SEM image (Fig. S12b), which strongly demonstrates the uniform deposition from the interconnected nanofibers to the whole Ni@PCNF-O composite membrane scale. Moreover, the Ni@PCNF-O composite exhibits much smoother and intact network structure with a recoverable fiber diameter of about 210 nm after stripping 8 mAh cm^{-2} of Li (Fig. $3f_3$) and extensive cycling (Fig. $3f_4$), while the uneven surface morphologies with multiple accumulated and isolated dead Li are observed for the Cu foil (Fig. S10d and S13) and Ni@CNF composite without original fibrous structure (Fig. $3e_3$ and $3e_4$). The obvious morphological difference in macro/micro scales strongly proves the efficiency of introducing oxygen-containing groups and rich mesoporous structure into the Ni@PCNF-O framework in tuning E-field distribution for uniform nucleation and subsequent growth of dendrite-free Li metal anode.

The electrochemical performances of repeated Li plating/stripping on different substrates are further tested in the coin-cell configurations. As depicted in Fig. 4a, the initial nucleation overpotentials are measured by galvanostatic charge/discharge (GCD) curves at a current density of 0.5 mA cm^{-2}. The Ni@PCNF-O electrode renders a much lower nucleation overpotential (10 mV) than those of Cu foil (48 mV) and bare

Ni@CNF electrode (21 mV), implying the positive effects of Ni@PCNF-O composite on guiding the initial Li metal nucleation. The Coulombic efficiency (CE), defined as the ratio of Li stripping capacity to plating capacity, is considered as an indicator to evaluate the reversibility of Li metal anodes in half-cells [42]. As depicted in Fig. 4b, at a current density of 0.5 mA cm^{-2} and capacity of 1.0 mAh cm^{-2}, the CE of Cu foil drops to below 85% within 70 cycles, manifesting a poor cycling performance similar to the previous reports [43-45]. The Ni@CNF electrode exhibits better performance over Cu foil due to its 3D interconnected conductive network with low local current density, but still provides limited cycle life with declined CE after 170 cycles. Impressively, the CE of the Ni@PCNF-O electrode increases from 95.4% (1^{st} plating cycle) to 98.1% (10^{th} plating cycle), and remains stable at about 99.3% over 400 cycles (≈1600 h). The voltage *versus* areal capacity curves of Li plating/stripping on Ni@PCNF-O, Ni@CNF and Cu electrodes are presented in Fig. S14. As for the Ni@PCNF-O electrode, the curves of different cycles are almost coincident, which is consistent with the high CEs of above 99%, indicating the excellent reversibility upon cycling process. Whereas for the Cu foil, the Li stripping capacity is significantly less than the plating capacity after 100 cycles, which signifies the large irreversible capacity loss owing to the formation of dendritic and dead Li. Moreover, the Ni@PCNF-O electrode exhibits a low and stable voltage hysteresis of ≈ 23 mV for more than 400 cycles, much smaller than ≈ 40 mV hysteresis for Ni@CNF and ≈ 70 mV for Cu foil (Fig. 4c). Such merit is more prominent at higher current densities and larger capacities. As shown in Fig. S15 and S16, the Ni@PCNF-O electrode shows outstanding cycling

stability with much smaller voltage hysteresis. Even when cycled at 2 mA cm^{-2} for 4 mAh cm^{-2}, the Ni@PCNF-O electrode can run for 100 cycles with a final CE of 98.7% (Fig. 4d), which confirms that the dendrite-free growth behavior and outstanding structure integrity of Ni@PCNF-O electrode can efficiently improve lithium utilization during the cycling process. Besides, the CE stabilities of Ni@PCNF and Ni@CNF-O electrodes are also improved in different degrees (Fig. S17). The CE tests are further measured under step-increased current density from 0.5 to 3.5 mA cm^{-2} and capacity from 1 to 20 mAh cm^{-2} in Fig. 4e and 4f. The CE of Ni@CNF electrode starts to oscillate drastically over the current density of 3 mA cm^{-2} or the capacity of 8 mAh cm^{-2}, while the Cu foil electrode has already failed at lower current density or capacity. On the contrary, the Ni@PCNF-O electrode displays high CE retention even at a high current density of 3.5 mA cm^{-2} (Fig. 4e) or a large deposition capacity of 20 mAh cm^{-2} (Fig. 4f), demonstrating the excellent rate performance and high loading capability of the Ni@PCNF-O electrode.

Apart from the CE test, symmetric cells are assembled by Ni@PCNF-O with pre-deposited 3 mAh cm^{-2} Li to evaluate the long-term electrochemical stability. The voltage-time profiles of Ni@PCNF-O@Li, Ni@CNF@Li and bare Li foil symmetric cells at 0.5 mA cm^{-2} for 1 mAh cm^{-2} are exhibited in Fig. 4g, which shows that the symmetric cell with Li foil displays the largest voltage overpotential of about 250 mV. Furthermore, the voltage hysteresis starts to increase only after 50 h for Li foil, accompanied by the random voltage vacillations, which can be attributed to the formation of unstable SEI layer and severe Li dendrites in the cell. When the Ni@CNF

composite is used as the Li metal host, the cell shows an improved performance with around 400 h of stable cycles before failure. Remarkably, the Ni@PCNF-O@Li symmetric cell displays a consistent overpotential of 17 mV and achieves ultra-long lifespan over 1200 h (300 cycles). The inset of Fig. 4g also clearly reveals that the voltage profiles of Ni@PCNF-O@Li still integrally remain the shape with regular and flat plateaus during 250 cycles, verifying the steady interfacial property of Ni@PCNF-O composite due to the buffered 3D structure and uniform plating/stripping behavior. To further demonstrate the superior electrochemical stability of Ni@PCNF-O composite, comparisons of the symmetric cell performance at higher current densities are obtained. Under the circumstance that Li dendrites are more likely to form by high-rate deposition, the Ni@PCNF-O@Li electrode can still present a stable and lower voltage hysteresis even under 6 mA cm^{-2} (Fig. 4h and Fig. S18), whereas higher overpotential and faster short-circuit can be detected in the cases of both Ni@CNF@Li and bare Li symmetric cells. Therefore, the results of CE test and symmetric cells for Ni@PCNF-O electrode, which precede many previous works of designed anode materials (Table S1 and S2), reconfirm the important roles of tuning E-field distribution from the whole electrode to interconnected nanofiber scales in guiding Li metal deposition. Thus, greatly improved reversibility of Li plating/stripping and structural stability upon long-term cycling can be achieved for high-performance lithium metal batteries.

2.4 LiPSs Immobilization for Ni@PCNF-O Composite

Benefiting from the mesoporous carbon skeleton with multiple adsorptive sites, the

Ni@PCNF-O composite is also employed as the elemental sulfur host to effectively inhibit the shuttle effect. To verify the improved interaction with LiPSs contributed by mesopores and polar oxygen groups on the nanofiber surface, the visual adsorption results are presented in Fig. 5a. Compared with that of Ni@CNF composite, the Li_2S_6 solution with Ni@PCNF-O composite become colorless after soaking for 12 h. Nevertheless, the color of Li_2S_6 solutions with Ni@PCNF and Ni@CNF-O composites still remains slight yellow, suggesting the superior affinity of Ni@PCNF-O composite toward LiPSs. The Li_2S nucleation measurements in Fig. S19 also indicate the efficient catalytic activity of Ni@PCNF-O composite in the accelerated conversion dynamics from LiPSs to solid Li_2S. Given the homogeneous dispersion of sulfur and strong immobilization of Ni@PCNF-O, the incorporation of active sulfur has been achieved by dropping Li_2S_6 catholyte onto the Ni@PCNF-O composite to obtain Ni@PCNF-O@Li_2S_6 electrode. Uniform nanoparticles cover the surface of Ni@PCNF-O nanofibers according to the SEM images (Fig. S20a and S20b). Furthermore, the uniform distribution of S element signal in the EDS mapping confirms the successful diffusion of Li_2S_6 into the electrode (Fig. S20c). For comparison, the S and carbon black (CB@S) mixture is prepared as a control sample (Fig. S21). Fig. 5b shows the typical cyclic voltammetry (CV) profiles of the Ni@PCNF-O@Li_2S_6 half-cell in the range of 1.7-2.8 V under various scan rates. Two representative cathodic peaks (R_1 and R_2) can be attributed to the reduction of S_8 to higher-order Li_2S_n ($4 \leq n \leq 8$) and the further reduction of the long-chain Li_2S_n to solid-state Li_2S_2, eventually to Li_2S. The anodic peak (O_1) is ascribed to the oxidation of Li_2S/Li_2S_2 to polysulfides and then to sulfur.

Correspondingly, the GCD curves of Ni@PCNF-O@Li_2S_6 half-cell at various current densities are shown in Fig. 5c. All the curves present distinct plateaus during the discharge/charge process, which is consistent with the prior CV results as representative phenomenon for Li-S batteries. Even at high current rates, the plateaus of GCD curves are well maintained because of the efficient LiPSs immobilization. Fig. 5d shows the rate capabilities of Ni@PCNF-O@Li_2S_6, Ni@CNF@Li_2S_6 and CB@S half-cells. Among them, the Ni@PCNF-O@Li_2S_6 half-cell exhibits 1611, 1270, 1119, 1001 and 888 mAh g^{-1} at 0.1, 0.2, 0.5, 1.0 and 2.0 C, respectively. Meanwhile, a high discharge capacity of 1011 mAh g^{-1} is still maintained when the current density returns to 1.0 C, implying the excellent structural integrity and chemical stability of the electrode material. The superior capacity at high current densities compared with Ni@CNF@Li_2S_6 and CB@S electrodes, is believed to be contributed to the stronger physical/chemical absorptivity in the Ni@PCNF-O@Li_2S_6 electrode. The Ni@PCNF@Li_2S_6 and Ni@CNF-O@Li_2S_6 half-cells also exhibit better rate capacities than that of Ni@CNF@Li_2S_6 (Fig. S22), indicating the enhanced immobilization of LiPSs from the chemical adsorption of oxygenated groups and physical confinement of mesopores within the oxygen-functionalized porous carbon nanofiber matrix. Simultaneously, the Ni@PCNF-O@Li_2S_6 half-cell delivers a high initial capacity of 1206 mAh g^{-1} at 0.2 C and still maintains 1080 mAh g^{-1} with nearly 100% CE over 100 cycles (Fig. S23). The long cycling stability is also investigated at 1.0 C (Fig. 5e). Remarkably, as for Ni@PCNF-O@Li_2S_6 half-cell, a high capacity of 951 mAh g^{-1} and a retention of 97.6% can still be retained after 300 cycles. In contrast, the

Ni@CNF@Li_2S_6 and CB@S half-cells demonstrate discharge capacities of only 498 and 190 mAh g^{-1} after 300 cycles with low retentions of 63.7% and 42.9%, respectively. The dramatic drop of capacity is also intuitively shown in the discharge/charge curves (Fig. S24), where the second discharge plateaus of Ni@CNF@Li_2S_6 become significantly shorter after cycling. Nonetheless, the Ni@PCNF-O@Li_2S_6 half-cell still delivers an initial discharge capacity of 820 mAh g^{-1} and a high capacity retention of 81.8% after 500 cycles at 2.0 C due to the successful anchoring of LiPSs through physical/chemical confinement (Fig. S25). This can be also ascribed to the smaller internal resistance and charger transfer resistance of Ni@PCNF-O@ Li_2S_6 half-cell over CB@S half-cell (Fig. S26).

To validate the potential of Ni@PCNF-O based Li-S cells for practical applications, the free-standing Ni@PCNF-O@Li_2S_6 electrodes with high-areal sulfur loading has been fabricated by dropping more Li_2S_6 [46-47]. As shown in Fig. S27, the Ni@PCNF-O@Li_2S_6 electrodes at areal S loadings of 1.8 mg cm^{-2} and 4.0 mg cm^{-2} exhibit reversible areal capacities of 2.4 mAh cm^{-2} and 4.9 mAh cm^{-2} at 0.1 C, respectively. Even under a high current density of 1.0 C, the Ni@PCNF-O@Li_2S_6 cathodes with 1.8 mg cm^{-2} and 4.0 mg cm^{-2} of S can still achieve stable cycling for 100 cycles with a high areal capacity of 1.6 mAh cm^{-2} and 3.2 mAh cm^{-2} respectively (Fig. 5f), which implies that the high-areal sulfur loading cells of Ni@PCNF-O electrode can still realize high sulfur utilization and excellent electrochemical performance.

2.5 Electrochemical Performance of Li-S Full Batteries

Ultimately, the Ni@PCNF-O@Li_2S_6 cathode and Ni@PCNF-O@Li anode are

assembled as a Li-S full battery, which is denoted as Ni@PCNF-O@Li_2S_6 || Ni@PCNF-O@Li, to evaluate the electrochemical performance (Fig. 6a). As shown in Fig. 6b, the Ni@PCNF-O@Li_2S_6 || Ni@PCNF-O@Li full battery with a low N/P of 2.0 presents the same typical discharge/charge curves as the previously studied Ni@PCNF-O@Li_2S_6 half-cell, meaning that no other side reactions occur in the whole reaction process. Motivated by the superiority of Ni@PCNF-O composite membrane as flexible hosts for both S cathode and Li metal anode, the Ni@PCNF-O@Li_2S_6 || Ni@PCNF-O@Li full battery exhibits higher capacities of 1616, 1372, 1184, 1042, 882 mAh g^{-1} at 0.1, 0.2, 0.5, 1.0 and 2.0 C respectively, compared to the commercial CB@S || Li full battery (Fig. 6c). The cyclability of these full batteries at a high current density of 1.0 C is further tested for 300 cycles in Fig. 6d and S28. The initial capacity of the Ni@PCNF-O@Li_2S_6 || Ni@PCNF-O@Li full battery is 1011 mAh g^{-1} and preserves a high capacity of 996 mAh g^{-1} over 300 cycles (capacity retention of 98.5%) with a high CE of nearly 100%, which is superior to most of the recently reported bifunctional hosts for Li-S full batteries (Table S3). In comparison, the routine CB@S || Li full battery initially exhibits the capacity of 454 mAh g^{-1} but only retains 193 mAh g^{-1} after 300 cycles, with a rapid capacity decay rate of 0.14% per cycle which is much faster than that (0.005%) of the Ni@PCNF-O@Li_2S_6 || Ni@PCNF-O@Li full battery. Remarkably, the capacity retention (98.5%) can be similar to the Ni@PCNF-O@Li_2S_6 half-cell which coupled with Li foil anode (97.6%), although the much less pre-plated Li (3 mAh cm^{-2}) than Li foil (≈ 100 mAh cm^{-2}). Moreover, the Ni@PCNF-O@Li_2S_6 || Ni@PCNF-O@Li full battery displays a high discharge capacity of 752 mAh g^{-1} over 500 cycles

with nearly 100% Coulombic efficiency and capacity retention of 90.1% (Fig. S29), indicating a high sulfur utilization and outstanding cyclic stability. Attributed to the highly flexible characteristic of Ni@PCNF-O electrode, a home-made bendable Ni@PCNF-O@Li_2S_6 || Ni@PCNF-O@Li pouch cell has been attained and repeatedly discharged/charged at different bending angles for 50 cycles at 0.2 C (Fig. 6e and 6f), indicating its good mechanical flexibility and commercial potentials in wearable and portable storage applications.

3. Conclusion

In summary, an oxygen functionalized three-dimensional mesoporous carbon nanofiber framework with well-distributed nickel nanoparticles (Ni@PCNF-O) has been rationally designed for dendrite-free Li metal anode and LiPSs-anchored cathode, simultaneously. As the lithium host, *COMSOL* simulation and experimental results demonstrate that the introduced oxygen groups and mesoporous structure can tune the distribution of electric field and offer abundant nucleation sites for Li. This would eliminate the "top-growth" mode and regulate the uniform dendrite-free Li deposition from the whole membrane electrode to the interconnected nanofiber scales. As the sulfur host, LiPSs can be physically/chemically anchored in the oxygen-functionalized porous framework, markedly alleviating LiPSs shuttling and improving sulfur utilization. Owing to these structural superiorities, the assembled Li-S full batteries with a low N/P of 2.0 allow to deliver multi-scale uniform Li deposition, extraordinary rate performance (882 mAh g^{-1} at 2.0 C) and prominent cycling lifespan (98.5%

retention after 300 cycles). Furthermore, the flexible Li-S batteries also possess good mechanical integrity and electrochemical stability in different bending status. This work not only provides a promising design to overcome challenges from both anode and cathode in Li-S batteries, but also sheds light on the electric field regulation on Li plating behaviors for safe and high-energy Li metal electrochemistry.

4. Experimental Section

4.1 Materials

Polyacrylonitrile (PAN) with molecule weight (M_w) of 150, 000 was provided by Sigma-Aldrich, Inc. *N,N*-dimethyl formamide (DMF), zinc acetate ($Zn(CH_3COO)_2$) and nickel acetate ($Ni(CH_3COO)_2$) were received from Sinopharm Chemical Reagent Co., Ltd.

4.2 Fabrication of Ni@PCNF-O Composite Membrane

The oxygen functionalized three-dimensional mesoporous carbon nanofiber framework with well-distributed nickel nanoparticles was prepared by the electrospinning method, carbonization and oxygen microwave plasma treatment. Typically, PAN (1.0 g), zinc acetate (0.1 g) and nickel acetate (0.4 g) were added to 10 mL DMF solution and stirred for 4 h. The resultant precursor solution was electrospun at a high voltage of 17.5 kV and a liquid pump rate of 1 mL h^{-1}. Then, the sample was peeled off from the collector and pre-sintered in air at 250 °C for 2 h, followed by carbonization at 900 °C for 2 h in an argon (Ar) atmosphere to obtain the self-standing membrane consisting of nickel nanoparticle embedded mesoporous carbon nanofibers,

which was named as Ni@PCNF. The Ni@PCNF-O framework was yielded by treating Ni@PCNF under oxygen microwave plasma at a power of 160 W with 200 s. For comparison, Ni@CNF composite was also fabricated based on the above steps without the addition of $Zn(CH_3COO)_2$ and Ni@CNF-O composite was obtained by treating Ni@CNF under O_2 plasma.

4.3 Materials Characterization

Morphology of all the samples was observed with field-emission scanning electron microscope (FESEM, JSM 7500F) and field-emission transmission electron microscope (FETEM, Talos F200S). The crystalline phase was measured by X-ray diffraction (XRD, X'Pert PRO X-ray diffractometer, Cu K_α radiation). The surface characteristics were investigated by X-ray photoelectron spectroscopy (XPS, Thermo Scientific ESCALAB 250Xi equipped with Al Kα X-ray source). The surface area was determined by using nitrogen adsorption/desorption collected with a Quantachrome Autosorb-iQ/MP®XR system. The thermogravimetric analysis (TGA) was carried out on a NETZSCH TG209F1 Libra device. In-situ optical microscopies were carried out to visualize Li plating behavior within Ni@PCNF-O, Ni@CNF and Cu substrates at 4 mA cm^{-2} by adopting a special polytetrafluoroethylene cell device and a microscope camera (Belona, 200X-800X). The applied current density was set by using electrochemical working station.

Li_2S_6 adsorption tests: The 5 mM Li_2S_6 solution was prepared by mixing Li_2S and S at a molar ratio of 1:5 in 1,3-dioxolane/1,2-dimethoxyethane (DOL/DME) (1:1 in volume) solvent followed by continuous stirring in glove box. Ni@PCNF-O, Ni@CNF-

O, Ni@PCNF, Ni@CNF, and CNF membranes were added to 3 mL of Li_2S_6 solutions respectively, with the pure Li_2S_6 solution as blank sample. Digital photos were taken after soaking for 12 h.

4.4 Electrochemical Measurement

Lithium metal anode tests: The electrochemical performances of all samples were conducted using the CR2025 coin cells. The self-standing membranes of Ni@PCNF-O, Ni@PCNF, Ni@CNF-O, Ni@CNF composites were cut into round disks with a diameter of 16 mm, and employed as electrode materials while Celgard 2500 membrane was used as the separator and 1 M lithium bis(trifluoromethanesulfonyl) imide (LiTFSI) in DOL/DME (1:1 in volume) containing 2 wt% lithium nitrate ($LiNO_3$) was adopted as electrolyte. For the Coulombic efficiency measurement, half-cells were assembled using Li foil as the counter electrode. For the symmetric cell test, the Ni@PCNF-O electrodes with pre-plating 3 mAh cm^{-2} of Li were used as both electrodes to replace Li foil. The thickness of electrode materials was fixed at about 100 μm and 40 μL electrolyte was added to each battery. Commercial planar Cu foil and Ni@CNF electrode were also measured together with Ni@PCNF-O electrode for comparison. All the cells were operated via galvanostatic charge/discharge (GCD) at 0.5 mA cm^{-2} between 0.01 and 1 V for the initial three cycles to stabilize the SEI films and eliminate impurities in the cells.

Sulfur cathode tests: All the electrochemical tests were performed with CR2025 coin cells with the sulfur cathodes and lithium foils separated by Celgard 2500 separator. 1 M LiTFSI in a mixture of DOL and DME (1:1 in volume) with 2 wt% $LiNO_3$ was used

as the blank electrolyte. The polysulfide catholyte with 2.0 M Li_2S_6 was prepared by stirring stoichiometric sulfur and lithium sulfide (Li_2S) in the blank electrolyte for 24 h. Then, different volume of polysulfide solution was dropped onto the circular Ni@PCNF-O electrode with a diameter of 12 mm in an Ar-filled glove box to obtain the Ni@PCNF-O@Li_2S_6 cathode. The electrolyte/sulfur ratio was fixed at 14 μL mg^{-1}. The GCD tests were conducted by using a LAND CT2001A battery testing system at different current densities within a voltage window of 1.7-2.8 V. The active Li_2S_6 was converted to sulfur after the initial few cycles and all the capacity values were calculated according to the weight of sulfur in the cathodes. The cyclic voltametric (CV) tests were carried out with an Arbin BT2000 system and electrochemical impedance spectroscopy (EIS) was measured by using a CHI660C electrochemistry workstation over the frequency range from 0.1 to 10^5 Hz.

Full Li-S batteries tests: Full Li-S batteries were assembled with Ni@PCNF-O@Li as the lithium anode and Ni@PCNF-O@Li_2S_6 as the sulfur cathode. Ni@PCNF-O@Li anodes were prepared by pre-depositing 3 mAh cm^{-2} of Li metal onto Ni@PCNF-O electrodes at 0.5 mA cm^{-2}. The sulfur cathodes and electrolyte were similar to that in the half-cells. The average sulfur mass of cathode used in this work was controlled around 0.9 mg cm^{-2}, and the negative to positive electrode capacity ratio (N/P) was about 2.0. The GCD tests were performed by using a LAND CT2001A battery testing system with the cut-off voltages of 1.7-2.8 V at room temperature.

4.5 Numerical Simulation

The finite element analysis simulations of the electric field and Li-ion flux

distribution within two different models were performed by *COMSOL* Multiphysics. The first was a simplified 3D model of randomly arranged Ni@CNF and Ni@CNF-O fibers, where the fibers of each layer with an alternating direction were stacked horizontally on the X-Y plane, and the spacing on the Z-axis of neighboring layer was fixed. The second model simulated the porous structure on a single fiber after simplified and unified processing. In the above two simulations, the initial electrolyte concentration (C_0) was set as 500 mol m^{-3} (0.5 mol L^{-1}) and the Li^+ diffusion coefficient was set to 1.5×10^{-10} m^2 s^{-1}.

Declaration of competing interest

The authors declare no conflict of interest.

Acknowledgements

The authors are grateful for the financial support from the National Natural Science Foundation of China (22075042), Natural Science Foundation of Shanghai (20ZR1401400, 18ZR1401600), the Shanghai Scientific and Technological Innovation Project (18JC1410600), the Fundamental Research Funds for the Central Universities and DHU Distinguished Young Professor Program (LZB2021002).

Appendix A. Supplementary data

Supplementary data to this article can be found online at http:// doi.org/10.1016/j.ensm.

Reference

[1] Z. Wu, Y. Wang, X. Liu, C. Lv, Y. Li, D. Wei, Z. Liu, Carbon-nanomaterial-based flexible batteries for wearable electronics, Adv. Mater. 31 (2019) 1800716.

[2] H. Kim, W. Choi, J. Yoon, J.H. Um, W. Lee, J. Kim, J. Cabana, W.S. Yoon, Exploring anomalous charge storage in anode materials for next-generation Li rechargeable batteries, Chem. Rev. 120 (2020) 6934-6976.

[3] J.B. Goodenough, K.-S. Park, The Li-ion rechargeable battery: a perspective, J. Am. Chem. Soc. 135 (2013) 1167-1176.

[4] W. Zong, C. Yang, L.L. Mo, Y. Ouyang, H.L. Guo, L. Ge, Y.E. Miao, D. Rao, J. Zhang, F.L. Lai, T.X. Liu, Elucidating dual-defect mechanism in rhenium disulfide nanosheets with multi-dimensional ion transport channels for ultrafast sodium storage, Nano Energy 77 (2020) 105189.

[5] G. Li, S. Wang, Y. Zhang, M. Li, Z. Chen, J. Lu, Revisiting the role of polysulfides in lithium-sulfur batteries, Adv. Mater. 30 (2018) 1705590.

[6] P.G. Bruce, S.A. Freunberger, L.J. Hardwick, J.-M. Tarascon, Li-O_2 and Li-S batteries with high energy storage, Nat. Mater. 11 (2012) 19-29.

[7] X.B. Zhu, Y. Ouyang, J.W. Chen, X.G. Zhu, X. Luo, F.L. Lai, H. Zhang, Y.E. Miao, T.X. Liu, In situ extracted poly(acrylic acid) contributing to electrospun nanofiber separators with precisely tuned pore structures for ultra-stable lithium-sulfur batteries, J. Mater. Chem. A 7 (2019) 3253-3263.

[8] D. Lin, Y. Liu, Y. Cui, Reviving the lithium metal anode for high-energy batteries, Nat. Nanotechnol. 12 (2017) 194-206.

[9] D. Wang, W. Zhang, W. Zheng, X. Cui, T. Rojo, Q. Zhang, Towards high-safe lithium metal anodes: suppressing lithium dendrites via tuning surface energy, Adv. Sci. 4 (2017) 1600168.

[10] T. Zhang, H. Lu, J. Yang, Z. Xu, J. Wang, S.-i. Hirano, Y. Guo, C. Liang, Stable lithium metal anode enabled by a lithiophilic and electron/ion conductive framework, ACS Nano 14 (2020) 5618-5627.

[11] S.H. Chung, A. Manthiram, Rational design of statically and dynamically stable lithium-sulfur batteries with high sulfur loading and low electrolyte/sulfur ratio, Adv. Mater. 30 (2017) 1705951.

[12]P. Quan, S. Abhinandan, N. Badri, K.C. Yuen, L.A. Curtiss, L.F. Nazar, Tuning the electrolyte network structure to invoke quasi-solid state sulfur conversion and suppress lithium dendrite formation in Li-S batteries, Nat. Energy 3 (2018) 783-791.

[13]X.F. Wang, Y. Qian, L.N. Wang, H. Yang, H.L. Li, Y. Zhao, T.X. Liu, Sulfurized polyacrylonitrile cathodes with high compatibility in both ether and carbonate electrolytes for ultrastable lithium-sulfur batteries, Adv. Funct. Mater. 29 (2019) 1902929.

[14]Y. Sun, N. Liu, Y. Cui, Promises and challenges of nanomaterials for lithium-based rechargeable batteries, Nat. Energy 1 (2016) 16071.

[15]X.B. Cheng, R. Zhang, C.Z. Zhao, Q. Zhang, Toward safe lithium metal anode in rechargeable batteries: a review, Chem. Rev. 117 (2017) 10403-10473.

[16]R. Zhang, N.W. Li, X.B. Cheng, Y.X. Yin, Q. Zhang, Y.G. Guo, Advanced micro/nanostructures for lithium metal anodes, Adv. Sci. 4 (2017) 1600445.

[17]C. Niu, H. Pan, W. Xu, J. Xiao, J.G. Zhang, L. Luo, C. Wang, D. Mei, J. Meng, X. Wang, Z. Liu, L.Q. Mai, J. Liu, Self-smoothing anode for achieving high-energy lithium metal batteries under realistic conditions, Nat. Nanotechnol. 14 (2019) 594-601.

[18]J. Tang, L. Hou, T. Hu, S. Fan, X. Zhou, J. Yang, Influence of oxygen content on the electrochemical behavior of SiO_x@C anodes for Li-ion battery, Compos. Commun. 23 (2021) 100544.

[19]X. Gu, C. Lai, One dimensional nanostructures contribute better Li-S and Li-Se batteries: progress, challenges and perspectives, Energy Storage Mater. 23 (2019) 190-224.

[20]J. Lei, T. Liu, J. Chen, M. Zheng, Q. Dong, Exploring and understanding the roles of Li_2S_n and the strategies to beyond present Li-S batteries, Chem 6 (2020) 2533-2557.

[21]M. Zhang, W. Chen, L. Xue, Y. Jiao, T. Lei, J. Chu, J. Huang, C. Gong, C. Yan, Y. Yan, Y. Hu, X. Wang, J. Xiong, Adsorption-catalysis design in the lithium-sulfur battery, Adv. Energy Mater. 10 (2020) 1903008.

[22]Z. Yuan, H.J. Peng, T.Z. Hou, J.Q. Huang, C.M. Chen, D.W. Wang, X.B. Cheng, F. Wei, Q. Zhang, Powering lithium-sulfur battery performance by propelling polysulfide redox at sulfiphilic hosts, Nano Lett. 16 (2016) 519-527.

[23] X. Hu, Z. Li, J. Chen, Flexible Li-CO_2 batteries with liquid-free electrolyte, Angew. Chem., Int. Ed. 56 (2017) 5785-5789.

[24] K.K. Fu, J. Cheng, T. Li, L. Hu, Flexible batteries: from mechanics to devices, ACS Energy Lett. 1 (2016) 1065-1071.

[25] F. Zhou, H. Huang, C. Xiao, S. Zheng, X. Shi, J. Qin, Q. Fu, X. Bao, X. Feng, K. Müllen, Z. Wu, Electrochemically scalable production of fluorine-modified graphene for flexible and high-energy ionogel-based microsupercapacitors, J. Am. Chem. Soc. 140 (2018) 8198-8205.

[26] W. Zong, N. Chui, Z. Tian, Y. Li, C. Yang, D. Rao, W. Wang, J. Huang, J. Wang, F. Lai, T. Liu, Ultrafine MoP nanoparticle splotched nitrogen-doped carbon nanosheets enabling high-performance 3D-printed potassium-ion hybrid capacitors, Adv. Sci. 8 (2021) 2004142.

[27] T.T. Zuo, X.W. Wu, C.P. Yang, Y.X. Yin, H. Ye, N.W. Li, Y.G. Guo, Graphitized carbon fibers as multifunctional 3D current collectors for high areal capacity Li anodes, Adv. Mater. 29 (2017) 1700389.

[28] Y. Fu, H. Zhou, Z. Hu, S. Yin, L. Zhou, Temperature-induced microstructure optimization of Co_3O_4 for the achievement of a high-areal-capacity carbon cloth-based lithium ion battery anode, Compos. Commun. 22 (2020) 100446.

[29] J. Li, P. Zou, S.W. Chiang, W. Yao, Y. Wang, P. Liu, C. Liang, F. Kang, C. Yang, A conductive-dielectric gradient framework for stable lithium metal anode, Energy Storage Mater. 24 (2020) 700-706.

[30] Z.L. Xu, J.K. Kim, K. Kang, Carbon nanomaterials for advanced lithium sulfur batteries, Nano Today 19 (2018) 84-107.

[31] X.-Y. Yue, X.-L. Li, W.-W. Wang, D. Chen, Q.-Q. Qiu, Q.-C. Wang, X.-J. Wu, Z.-W. Fu, Z. Shadike, X.-Q. Yang, Y.-N. Zhou, Wettable carbon felt framework for high loading Li-metal composite anode, Nano Energy 60 (2019) 257-266.

[32] R. Zhou, Y. Li, Y. Feng, C. Peng, W. Feng, The electrochemical performances of fluorinated hard carbon as the cathode of lithium primary batteries, Compos. Commun. 21 (2020) 100396.

[33] L. Liu, Y.X. Yin, J.Y. Li, N.W. Li, X.X. Zeng, H. Ye, Y.G. Guo, L.J. Wan, Free-

standing hollow carbon fibers as high-capacity containers for stable lithium metal anodes, Joule 1 (2017) 563-575.

[34] P. Zou, S. W. Chiang, J. Li, Y. Wang, X. Wang, D. Wu, A. Nairan, F. Kang, C. Yang, Ni@Li_2O co-axial nanowire based reticular anode: tuning electric field distribution for homogeneous lithium deposition, Energy Storage Mater. 18 (2019) 155-164.

[35] J. Yun, B.-K. Park, E.-S. Won, S.H. Choi, H.C. Kang, J.H. Kim, M.-S. Park, J.-W. Lee, Bottom-up lithium growth triggered by interfacial activity gradient on porous framework for lithium-metal anode, ACS Energy Lett. 5 (2020) 3108-3114.

[36] J. Pu, J. Li, K. Zhang, T. Zhang, C. Li, H. Ma, J. Zhu, P.V. Braun, J. Lu, H. Zhang, Conductivity and lithiophilicity gradients guide lithium deposition to mitigate short circuits, Nat. Commun. 10 (2019) 1896.

[37] S.H. Hong, D.H. Jung, J.H. Kim, Y.H. Lee, S.J. Cho, S.H. Joo, H.W. Lee, K.S. Lee, S.Y. Lee, Electrical conductivity gradient based on heterofibrous scaffolds for stable lithium-metal batteries, Adv. Funct. Mater. 30 (2020) 1908868.

[38] C. Chu, N. Wang, L. Li, L. Lin, F. Tian, Y. Li, J. Yang, S.X. Dou, Y. Qian, Uniform nucleation of sodium in 3D carbon nanotube framework via oxygen doping for long-life and efficient Na metal anodes, Energy Storage Mater. 23 (2019) 137-143.

[39] Y. Chen, M. Yue, C. Liu, H. Zhang, Y. Yu, X. Li, H. Zhang, Long cycle life lithium metal batteries enabled with upright lithium anode, Adv. Funct. Mater. 29 (2019) 1806752.

[40] Z. Liang, K. Yan, G. Zhou, A. Pei, J. Zhao, Y. Sun, J. Xie, Y. Li, F. Shi, Y. Liu, D. Lin, K. Liu, H. Wang, H. Wang, Y. Lu, Y. Cui, Composite lithium electrode with mesoscale skeleton via simple mechanical deformation, Sci. Adv. 5 (2019) eaau5655.

[41] L. Ye, M. Liao, T. Zhao, H. Sun, Y. Zhao, X. Sun, B. Wang, H. Peng, A sodiophilic interphase-mediated, dendrite-free anode with ultrahigh specific capacity for sodium-metal batteries, Angew. Chem., Int. Ed. 58 (2019) 17054-17060.

[42] C. Zhang, S. Liu, G. Li, C. Zhang, X. Liu, J. Luo, Incorporating ionic paths into 3D conducting scaffolds for high volumetric and areal capacity, high rate lithium-metal anodes, Adv. Mater. 30 (2018) 1801328.

[43] W. Fan, R. Zhang, Z. Wang, X. Lei, C. Qin, X. Liu, Facile fabrication of polyether

sulfone (PES) protecting layer on Cu foil for stable Li metal anode, Electrochim. Acta 260 (2018) 407-412.

[44] G. Li, Z. Liu, Q. Huang, Y. Gao, M. Regula, D. Wang, L.Q. Chen, D. Wang, Stable metal battery anodes enabled by polyethylenimine sponge hosts by way of electrokinetic effects, Nat. Energy 3 (2018) 1076.

[45] K.R. Adair, M. Iqbal, C. Wang, Y. Zhao, M.N. Banis, R. Li, L. Zhang, R. Yang, S. Lu, X. Sun, Towards high performance Li metal batteries: nanoscale surface modification of 3D metal hosts for pre-stored Li metal anodes, Nano Energy 54 (2018) 375-382.

[46] Z.L. Xu, S. Lin, N. Onofrio, L. Zhou, F. Shi, W. Lu, K. Kang, Q. Zhang, S.P. Lau, Exceptional catalytic effects of black phosphorus quantum dots in shuttling-free lithium sulfur batteries, Nat. Commun. 9 (2018) 4164.

[47] Z.L. Xu, N. Onofrio, J. Wang, Boosting the anchoring and catalytic capability of MoS_2 for high-loading lithium sulfur batteries, J. Mater. Chem. A 8 (2020) 17646-17656.

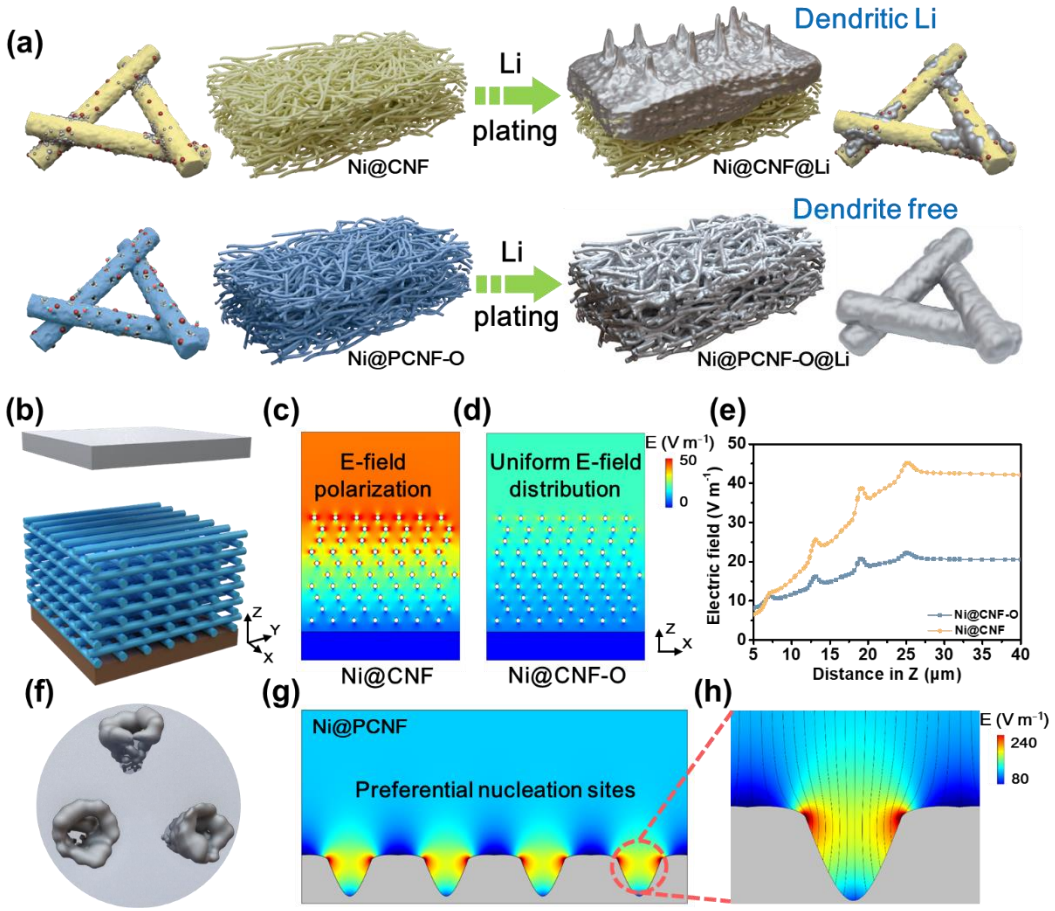

Fig. 1. Multi-scale uniform Li regulation by the oxygen-functionalized porous framework: (a) Schematic illustration of the Li plating behavior within Ni@CNF and Ni@PCNF-O composites. (b) *COMSOL* simulation model of Ni@CNF and Ni@CNF-O half-cell systems. Electric field distribution simulations and (e) the corresponding E-field profiles along Z directions in (c) Ni@CNF and (d) Ni@CNF-O electrodes. (f) Schematic showing the Li deposition into pore structure. (g) Electric field distribution simulations and (h) the corresponding Li ion flow lines in Ni@PCNF electrode.

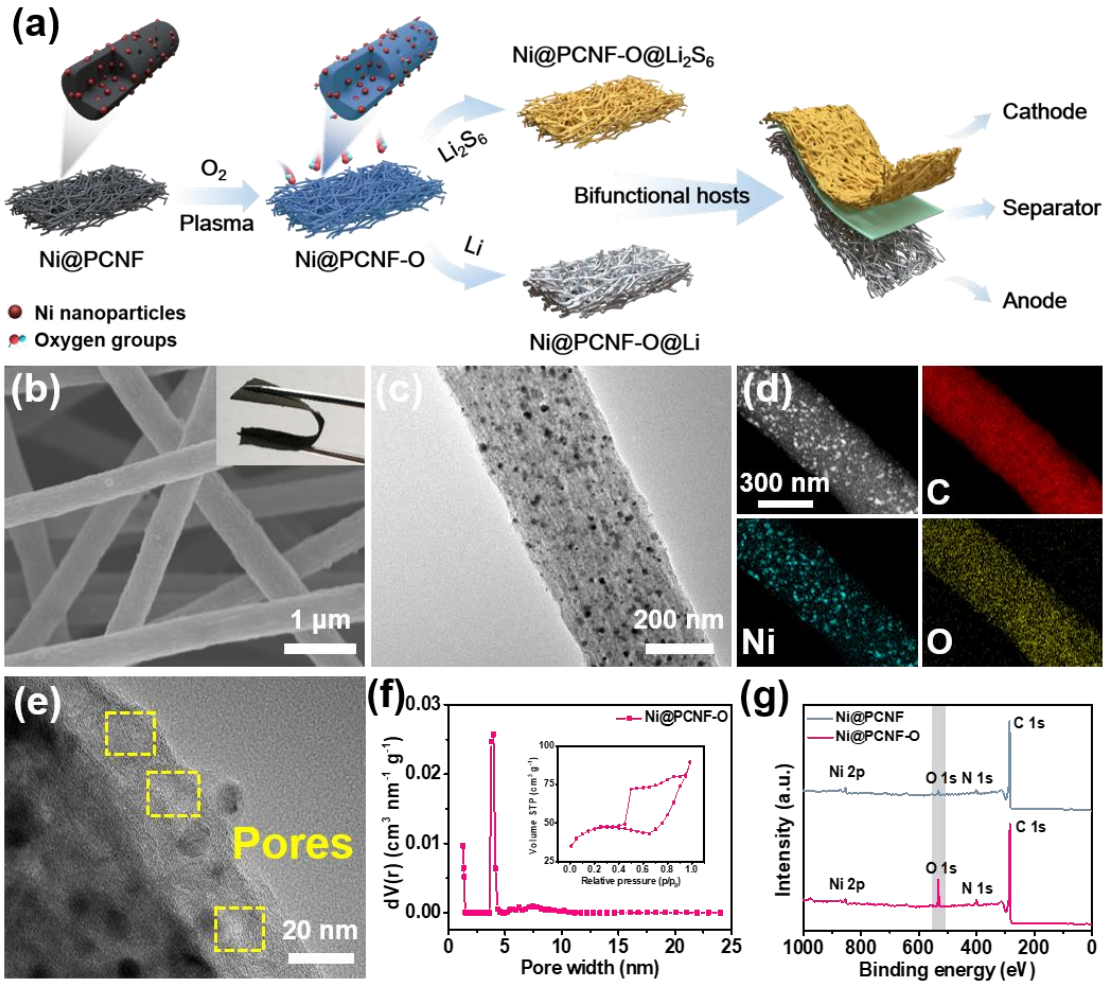

Fig. 2. (a) Schematic illustration of the synthetic procedure of Ni@PCNF-O composite. (b) SEM image, (c-e) TEM images and the corresponding EDX mappings, and (f) N_2 adsorption-desorption isotherm (inset) and pore size distribution of Ni@PCNF-O composite. (g) XPS spectra of Ni@PCNF and Ni@PCNF-O composites.

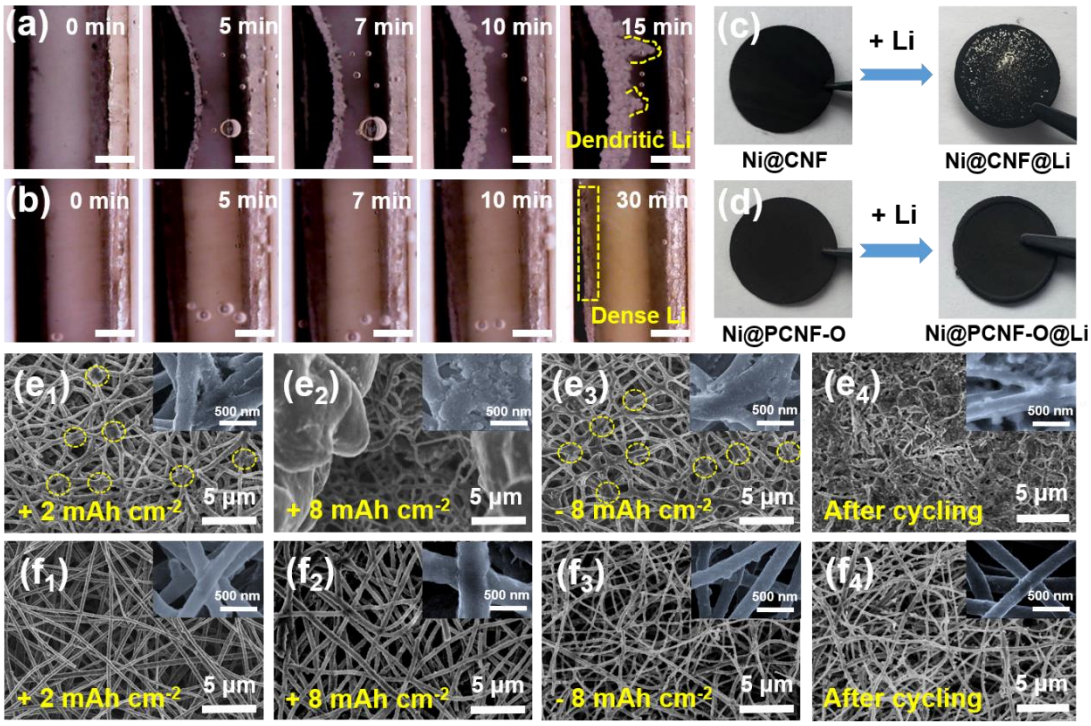

Fig. 3. Li metal plating/stripping behaviors in Ni@PCNF-O composite: Optical microscopy images of in-situ Li plating process in (a) Ni@CNF and (b) Ni@PCNF-O composites over time. Scale bar: 600 μm. The top-surface digital photos of (c) Ni@CNF and (d) Ni@PCNF-O composites before and after Li plating. SEM images of (e) Ni@CNF and (f) Ni@PCNF-O composites after plating/stripping of different capacities of Li: (e_1, f_1) + 2 mAh cm^{-2}, (e_2, f_2) + 8 mAh cm^{-2}, (e_3, f_3) - 8 mAh cm^{-2}, and (e_4, f_4) after 50 plating/stripping cycles of 2 mAh cm^{-2}.

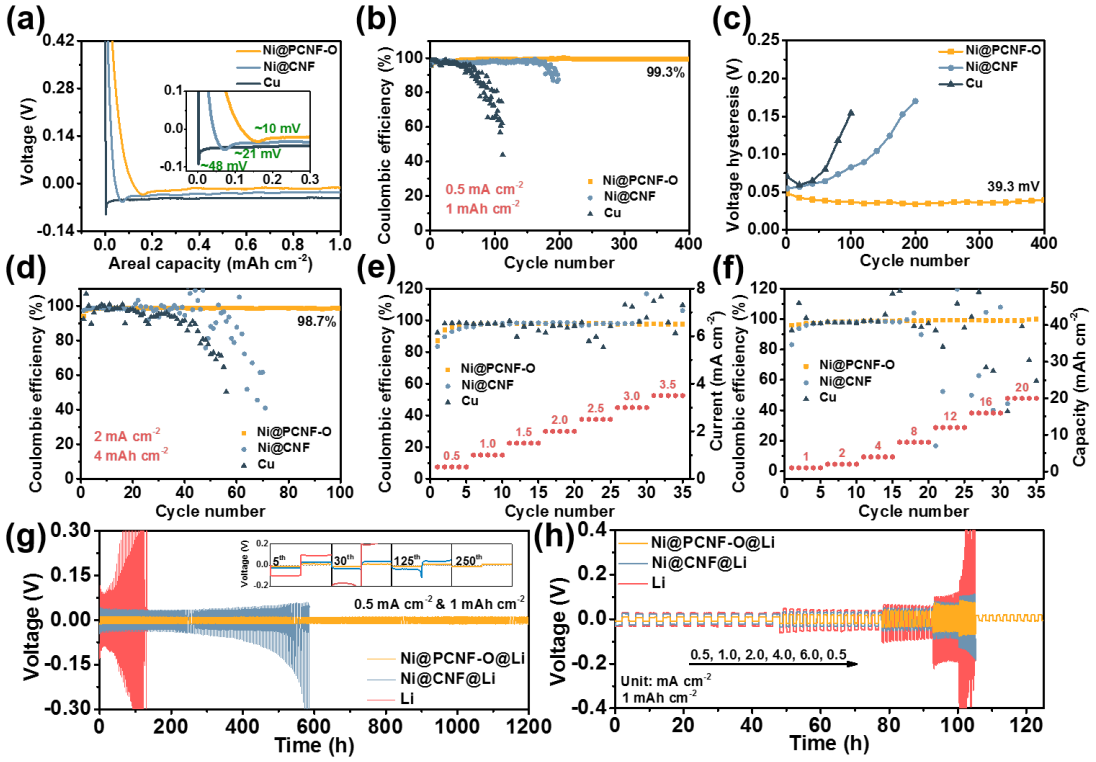

Fig. 4. (a) Voltage profiles of Li plating on different electrodes at 0.5 mA cm^{-2}. The inset shows the magnified nucleation overpotentials. (b) CE and (c) the corresponding voltage hysteresis of different electrodes at 0.5 mA cm^{-2} with the plating capacity of 1 mAh cm^{-2}. (d) CE profiles at 2 mA cm^{-2} with 4 mAh cm^{-2}. CE of different electrodes with increasing (e) current density and (f) capacity. Comparisons of (g) cycling performance and (h) rate performance of different electrode based symmetrical cells.

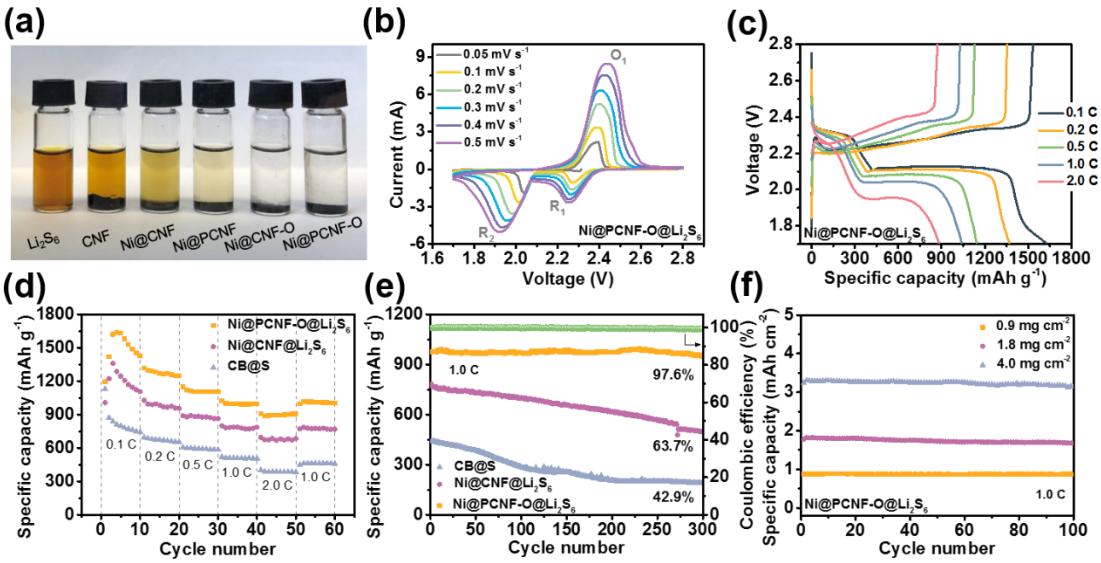

Fig. 5. LiPSs immobilization of Ni@PCNF-O composite: (a) Digital photographs of different samples after static adsorption of Li_2S_6. (b) CV curves under different scanning rates, and (c) Voltage profiles at various current densities of Ni@PCNF-O@Li_2S_6 half-cell. (d) Rate capabilities and (e) long-term cycling stability at 1.0 C of different half-cells. (f) Cycling performance of the Ni@PCNF-O@Li_2S_6 half-cells with different sulfur loadings at 1.0 C.

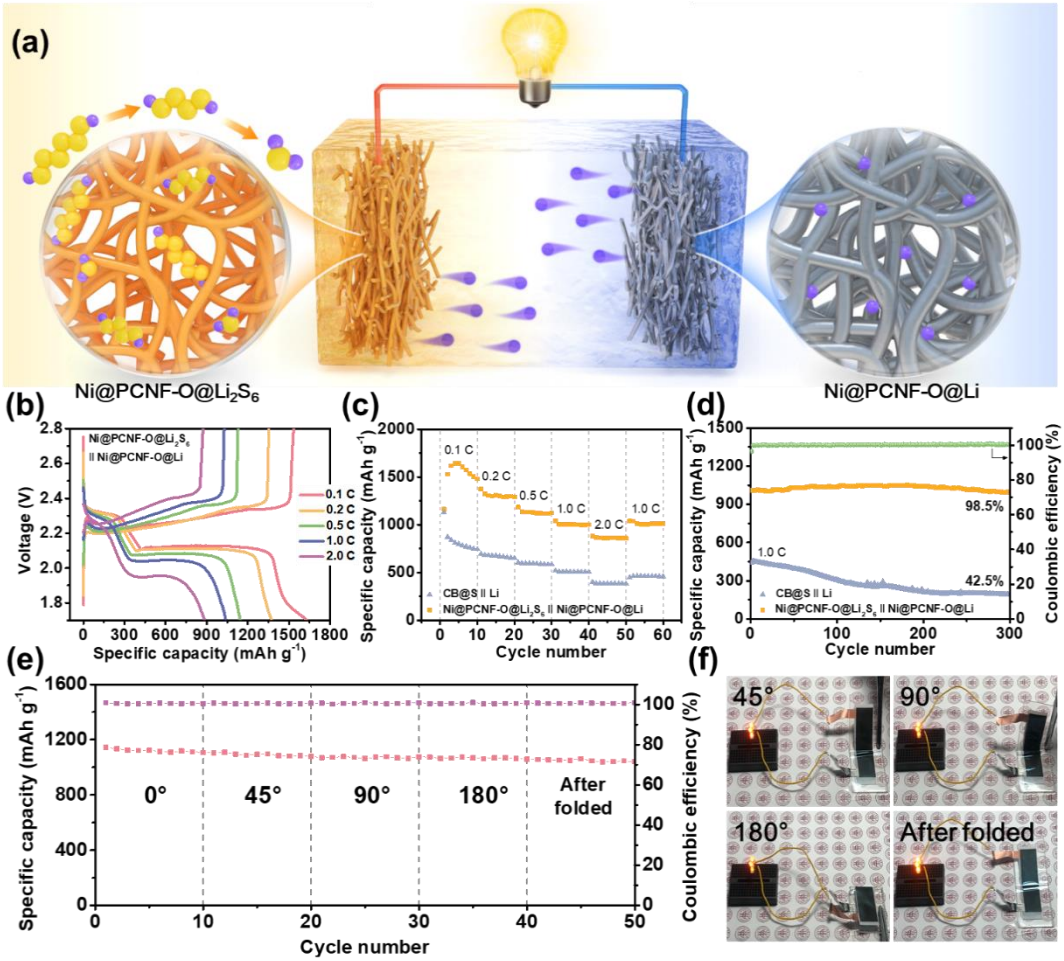

Fig. 6. Electrochemical performance of the flexible Li-S full batteries: (a) Scheme of the Li-S full battery with Ni@PCNF-O@Li_2S_6 as cathode and Ni@PCNF-O@Li as anode. (b) Voltage profiles at various current densities of Ni@PCNF-O@Li_2S_6 || Ni@PCNF-O@Li full battery. (c) Rate capabilities and (d) cycling performance of Ni@PCNF-O@Li_2S_6 || Ni@PCNF-O@Li and CB@S || Li full batteries. (e) Cycling performance at 0.2 C and (f) illuminating tests of Ni@PCNF-O@Li_2S_6 || Ni@PCNF-O@Li flexible pouch cell in various folded states.